Study of the ablation consecutive to jet impingement on a meltable solid – Application to SFR core-catcher

A. Lecoanet, F. Payot, C. Journeau, N. Rimbert, Michel Gradeck

Study of the ablation consecutive to jet impingement on a meltable solid - application to SFR core-catcher

A. Lecoanet[a,b], F. Payot[c], C. Journeau[a], N. Rimbert[b], M. Gradeck[b,*]

[a] *CEA, DES, IRESNE, Cadarache, DTN, SMTA, LEAG, F-13108 St Paul lès Durance, France*
[b] *Université de Lorraine, CNRS, LEMTA, F-54000, Nancy, France*
[c] *CEA, DES, IRESNE, Cadarache, DER, F-13108 St Paul lès Durance, France*

Abstract

In the scope of safety studies for future sodium cooled fast reactors (SFR-Na), the use of discharge tubes and in-vessel core-catcher are foreseen for severe accident mitigation. During relocation of corium onto the core-catcher, complex thermal hydraulics phenomena can occur. This work focuses on the ablation of the core-catcher by the corium's jet. For that purpose, as experiments using corium and Na are difficult to achieve, we performed experiments using simulant materials: water jet on transparent ice. Transparent ice allows for ablation cavity real-time recording. Two main regimes were identified : a film flowing regime and a pool regime. We also studied the influence of temperature (30, 50, 70 °C) and velocity (1, 2.5, 5, 7.5, 10 m/s) of the jet. Comparison with existing data have been done and finally, a scaling law in the first regime, for which the ablation rate is constant, has been found.

Keywords: Ablation, Liquid jet, core-catcher, corium-structure interaction, Sodium Fast Reactor, Pool effect

1. Nomenclature

Latin letters

*Corresponding author
Email address: michel.gradeck@univ-lorraine.fr (M. Gradeck)

B	Melting number	$\frac{C_{p,j}(T_{j,0}-T_{f,s})}{L+C_{p,s}(T_{f,s}-T_{s,0})}$	-
C	Velocity gradient in the stagnation zone	$\frac{V_j}{d}$	s^{-1}
C_p	Specific heat	-	$J.kg^{-1}.K^{-1}$
d	Jet diameter	-	m
g	Standard gravity	9.81	$m.s^{-2}$
h	Convective heat transfer coefficient	-	$W.m^{-2}.K^{-1}$
H	Jet drop height	-	m
k	Thermal conductivity	-	$W.m^{-1}.K^{-1}$
L	Latent heat of fusion	333 700 (ice [1])	$J.kg^{-1}$
m	Exponent over the Prandtl number	-	-
n	Exponent over the Reynolds number	-	-
Nu	Nusselt number	$\frac{hd}{k_j}$	-
Pr	Prandtl number	$\frac{\mu/\rho}{k/\rho C_p}$	-
r	Radial distance from jet axis	-	m
Re	Reynolds number	$\frac{\rho_j V d}{\mu_j}$	-
St	Stefan number	$\frac{C_{p,s}(T_{f,s}-T_{s,0})}{L}$	-
t	Time	-	s
t^*	Dimensionless time	$\frac{t}{t_{PE}}$	-
T	Temperature	-	K
V	Velocity	-	$m.s^{-1}$
We	Weber number	$\frac{\rho_j V^2 d}{\sigma_j}$	-
X	Dimensionless jet temperature number	Eq. (5)	
y	Dimensionless film thickness number	-	
Y	Dimensionless melting rate number	Eq. (6)	
z	Depth	-	m
Z^*	Relative depth at pool effect appearence	$\frac{z_{PE}}{d}$	-

Greek letters

Δ	Absolute uncertainty	-	-
μ	Dynamic viscosity	-	$Pa.s = kg.m^{-1}.s^{-1}$
ν	Kinematic viscosity	$\frac{\mu}{\rho}$	$m^2.s^{-1}$
ρ	Density	-	$kg.m^{-3}$
σ	Surface tension	-	$N.m^{-1}$

Indices

0	Initial / nozzle
1	Calculated using Eq. (15)
2	Computed using Sato *et al.* scaling law, Eq. (13)
e	Entrainment
eff	Effective (with fusion)
exp	Experimental (measured)
f	Fusion
i	Interface
imp	At impact
j	Jet
m	Layer of melted solid
PE	Pool effect
s	Solid
si	Swedish *et al.* [2] model

2. Glossary

$ASTRID$	Advanced Sodium Technological Reactor for Industrial Demonstration
$ESFR-SMART$	European Sodium Fast Reactor - Safety Measures Assessment and Research Tools
FCI	Fuel–Coolant Interaction
$HAnSoLO$	Hot AblatioN of a SOlid by a Liquid – Observations
IR	Infrared

$LEMTA$	*Laboratoire Énergies & Mécanique Théorique et Appliquée*
LT	Level Transmitter
NPP	Nuclear Power Plant
PE	Pool Effect
PT	Pressure Transmitter
PWR	Pressurized Water Reactors
SFR	Sodium Fast Reactor
TC	Temperature Controller
TT	Temperature Transmitter

3. Introduction

. Fourth generation of nuclear power plants (NPP) is under study. Two of the main objectives of this generation are (i) to reach safety levels beyond those of previous generation and (ii) to improve their sustainability [3]. Nuclear cores making use of fast neutrons spectrum are good candidates to meet the later goal. They can use ^{238}U which is unusable for pressurized water reactors (PWR) and accounts for about 99% of uranium resources [4]. Minor actinides transmutation is also feasible under fast neutron spectrum [3]. It could reduce ultimate waste's activity and half-life [4]. In order to maintain a fast neutron spectrum, the refrigerant must be transparent to neutrons and be able to transfer the heat from the fisible core. Among the best candidates is sodium. It has been used in the past so that feed-back is available. Sodium Fast Reactors (SFR) is thus one of the most studied type of fourth generation nuclear core. This study which is part of an european project called ESFR-SMART is intended to help design of future SFRs taking into account safety criteria.

. We learned from Fukushima's accident [5] that severe accident events with core meltdown[1] must be studied, and mitigation strategies must be defined. In case of core meltdown in SFR, a corium (mixture of nuclear fuel, fission products,

[1] O3 objective of WENRA statement on safety objectives for new NPP [5].

control rods, and steel structure elements) can form and the best strategy to reduce its thermal power, the risk of re-criticality and improve its later cooling and handling, is to relocate it outside of the core as soon as possible [6]. That is why discharge tubes are located in the reactor core; in case of meltdown, the corium can relocate down on a device called the core-catcher which is in the vessel lower head [6].

As a strong thermal interaction between the corium jet and the core-catcher is expected, namely an ablation that could lead to a perforation of it, we decided to deeply study this complex phenomenon using simulants to be able to understand more the course of the ablation.

Figure 1 gives a schematic explanation of the course of events.

Figure 1: (Left) Schematic cross-section of a pool-type SFR with discharge tubes and a core-catcher. (Right) ASTRID cross-section.

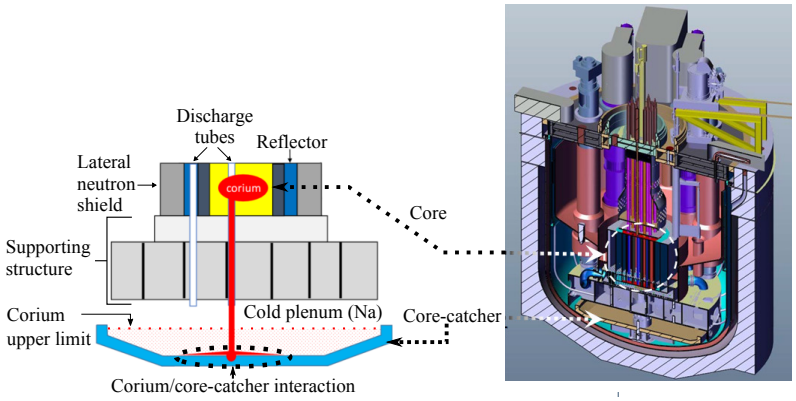

. During the relocation process, corium goes out by the orifice of the discharge tubes in the cold plenum of the vessel filled with sodium at 400 ^oC. Whatever the scenario, sodium surrounding the corium is expected to vaporize leading or not to a more or less important destabilization of the corium jet. So, different scenarii can be considered: (i) FCI without steam explosion leading to the atomization of corium's jet with relocation of the debris onto the core-catcher (this case is considered as favorable because the heat would be spread), (ii) coherent

jet formation and impact of it onto the core-catcher. This last scenario is considered as the most critical for containment as the heat would be concentrated in the zone of impact. In-vessel structures can also prevent large amounts of sodium vapor from flowing upward. These structures foster the second scenario. In this scenario, corium could thus flow as a free jet accelerated by gravity. As this second case is the worst of the two for safety reasons, it must be first considered for the design. In this paper, we only studied a free water jet impinging onto an ice block leading to its melting.

. Depending on the core-catcher material and composition of the corium, a crust can form during the thermal interaction between the jet and the solid. Even worthy of investigations, the situation leading to crust formation will thus not be considered in this study as it will reduce the heat transfer, and we are looking for studying the worst case for the design of core-catcher. When the corium is formed, it is mainly composed of oxides coming from the nuclear fuel and steel coming from structure elements. Oxides and metals composing the corium are not miscible. They segregate in two phases that can relocate one after the other. Therefore, two main classes of materials are considered for core-catcher, oxides (*i.e.* UO_2) and metals. When both the jet and the core-catcher are of similar composition (metal/metal or oxide/oxide), thermal power density heats core-catcher and can make it melt (Case n°1 Fig. 2) without crust formation or chemical reaction. When the core-catcher is metallic and the jet composed of oxide, a crust is thus likely to form [7] due to the difference between oxide solidification temperature and metal melting temperature (Case n°2 Fig. 2). The crust reduces the heat transfer but melting can still occur beneath it. Crust's stability depends mainly on its thermal [8] and mechanical properties [9].

When a jet impinges on a solid of same nature, the initial solid temperature can induce a delay in ablation start. This effect is only encountered when the contact temperature between the solid and the jet is below the temperature of solidification of the material of the jet. The contact temperature is estimated

through an exact solution of the heat equation when two infinite media, initially at a constant temperature are put in contact at $t = 0\ s$, Eq. (1). It is a function of solid and jet initial temperature, density ρ, specific heat C_p and thermal conductivity k.

$$T_0 = T_{0,s} + \frac{T_{0,j} - T_{0,s}}{1 + \sqrt{\frac{\rho_s C_{p,s} k_s}{\rho_j C_{p,j} k_j}}} \tag{1}$$

Figure 2: Possible ablative outcomes at impact of a free corium jet on a core-catcher. Important boundary conditions are indicated in the schematic for case n° 1.

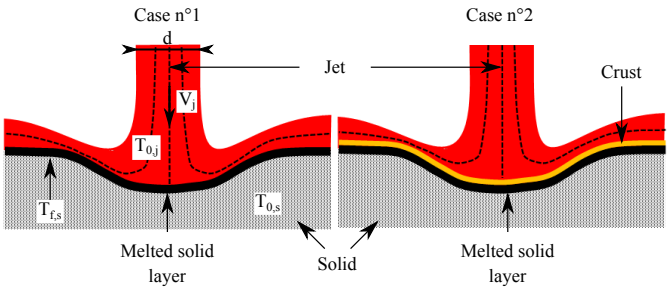

. Previous works studied ablation of a solid block impacted by a free jet. The first one that we can cite is a theoretical study by Roberts [10] who investigated the melting of ice impinged by a gas jet. The results are limited to the stagnation zone within which the boundary layers are of constant thickness. Over this zone the velocity of the fluid increases from 0 to V after impinging the solid perpendicularly. In the stagnation zone, the acceleration of the fluid is constant as the boundary layer thickness [11]. The velocity of the fluid evolves radially, see equation (2).

$$V = Cr \quad \text{with} \quad C = \frac{V_j}{d} \tag{2}$$

Two mechanisms of heat transfer reduction due to ablation were identified. The first is the decrease of temperature difference between jet, and its interface

with liquid melt layer. The second is convection within the melt layer. Epstein [12] proposed a procedure to adapt existing experimental scaling laws, obtained without considering the melting, to the case where melting occurs. A demonstration of this relation, when the solid is at its melting temperature, is provided by Tien *et al.* [13]. The Nusselt number with melting (Nu_f) is obtained from the one estimated with an experimental scaling laws without melting (Nu) using Eqs. (3) and (4). Melting number B (*cf.* Eq. (4)) was first introduced by Griffin [14]. In these equations, d is the jet diameter, k_j the jet thermal conductivity, h is the heat transfer coefficient if there is no melting, h_{eff} is the effective heat transfer coefficient with melting, $C_{p,j}$ is the heat capacity of the liquid coming from the jet, $C_{p,s}$ is the heat capacity of the solid, and L is the latent heat of fusion.

$$Nu = \frac{B}{ln\,(1+B)} Nu_f \qquad with \qquad Nu = \frac{hd}{k_j}, \qquad Nu_f = \frac{h_{eff} d}{k_j} \tag{3}$$

$$B = \frac{C_{p,j}\,(T_{0,j} - T_{f,s})}{L + C_{p,s}\,(T_{f,s} - T_{0,s})} \tag{4}$$

. Roberts' study [10] was expanded to the case of a liquid impacting jet, with the addition of experimental work by Furutani *et al.*[2] [15] and Swedish *et al.*[3] [2]. These studies focus on the stagnation zone.

In these models two layers of fluid are considered. The flow is considered laminar. The first layer corresponds to the fluid coming from the melting of the solid. The second one is the boundary layer present in the flow of liquid coming from the jet. The situation under study is represented in figure 3. When materials from the jet and the solid are not similar, radial velocity gradient is discontinuous between the two layers. According to Swedish *et al.* [2], the change of gradient is proportional to the square root of the density ratio in both layers. Nevertheless, the model of Swedish *et al.* [2] can still be applied

[2]Solid tested: two paraffins and Wood's metal impacted by water.

[3]Solid tested: ice, frozen octane, frozen olive oil and frozen p-xylene impinged on by water.

Figure 3: Schematic of the situation studied by Swedish *et al.* [2] adapted to our notation.

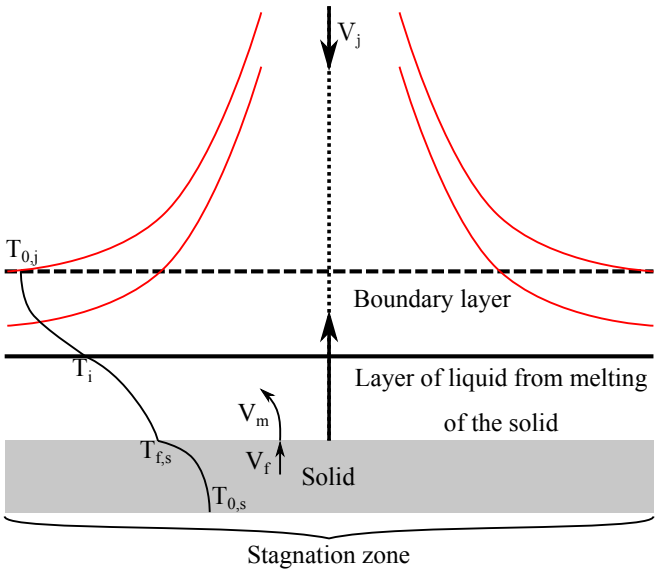

when both liquid layers are of the same nature. It is an approximate model in which the film of fluid coming from melting of the solid is assumed to be thin and the velocity profile in this film is considered to be linear. Swedish *et al.* [2] introduced two dimensionless numbers, X which is a dimensionless jet temperature number (Eq. (5)) and Y which is a dimensionless melting rate number (Eq. (6)).

$$X = 0.169 \left(\frac{k_j}{k_m}\right)^2 \left(\frac{\nu_m}{\nu_j}\right) B \tag{5}$$

$$Y = 0.306 \left(\frac{k_j}{k_m}\right)^2 \left(\frac{\nu_m}{\nu_j}\right) \left(\frac{\rho_s}{\rho_j}\right) Pr^2 \frac{V_f}{\sqrt{C\nu}} \tag{6}$$

We modified the expression of Y to take the jump condition over the mass into account. The jump condition over the mass (Eq. (7)) links the solid melting velocity – V_f – and the vertical velocity of fluid produced at the melting interface – V_m.

$$\rho_s V_f = \rho_m V_m \tag{7}$$

X and Y are linked by equation (8).

$$X = \frac{Y}{\sqrt{2}} \left[1 + \left(\frac{Y\sqrt{2}}{f''(0)} \right)^{1/2} \right] \Leftrightarrow X = \frac{1}{2} f''(0) \left(1 + y\right) y^2 \tag{8}$$

$$\frac{T_i - T_{f,s}}{T_{0,j} - T_{f,s}} = \frac{y}{1+y} \tag{9}$$

f is the dimensionless profile of vertical velocity. $f''(0)$ is the dimensionless shear stress at solid / liquid interface. Swedish *et al.* [2] give a value of 0.9277 for $f''(0)$. In these equations variables with m subscript refer to the properties of the fluid in the layer of melted solid.

Swedish *et al.* [2] introduced the interface temperature T_i (Eq. (9)) which is linked to the dimensionless jet temperature number X (Eq. (5)) by means of a film thickness number y (Eqs. (8) & (9)). The number y is a dimensionless measure of the thickness of the layer of liquid coming from the melting of the solid. To take the influence of temperature variation within the fluid layers into account, the fluid properties needed to compute X and Y can be estimated at $T = \frac{1}{2}\left(T_i + T_{f,s}\right)$ for the layer of melted solid, and at $T = \frac{1}{2}\left(T_i + T_{0,j}\right)$ for the boundary layer of fluid coming from the jet.

When both melt and jet have same composition, the density varies continuously. In this case, Swedish *et al.* [2] recommended, instead of solving the equation presented, to first estimate the Nusselt number without melting, then correct it to take melting into account by making use of Epstein's correction described before (Eqs. (3) and (4)). The effective Nusselt number taking melting into account – Nu_f – can then be used to assess the melting velocity using the following equation when there is no sub-cooling of the solid.

$$Nu_f = \frac{V_f \rho_s dL}{\left(T_{0,j} - T_{f,s}\right) k_j} \tag{10}$$

Swedish *et al.* [2] indicated that experimental scaling law determined by Sitharamayya *et al.* [16] (Eq. (11)) could be used to estimate the Nusselt number without melting.

$$Nu = 0.5077 Re^{0.523} Pr^{0.33} \tag{11}$$

The exponent over the Reynolds number is close to 1/2. The exponent over the Prandtl number is close to 1/3. These two values of 1/2 and 1/3 were also obtained theoretically for the stagnation zone of an axisymmetric laminar flow [17].

The approach making use of a correction of Nusselt scaling laws to take melting into account is also coherent with the work of Yen *et al.* [18] who noted a decrease in heat transfer due to melting even if no non-miscible melt layer is formed between the jet and the solid.

. Concerning ablation of a solid by a liquid jet of same composition, without intermediate immiscible melt layer, experimental works of Gilpin [19] and of Yen *et al.* [18] can be cited. They obtained valuable data, especially Gilpin who noted that solid surface smoothness plays an important role in ablation mechanism as two different ablation regimes can appear based on solid rugosity. The apparatus used in these studies were similar and the solid was impacted from below by an upward flowing free jet. In the stagnation zone where the jet impacts the solid, liquid is mainly deviated at right angle with respect to both jet axis and gravity. Therefore, the fact that the jet is directed downward or upward with respect to gravity should not play an important role as long as the change in jet velocity between the nozzle and target is taken into account. However, outside stagnation zone, where liquid spreads as a film, the two cases are not similar: in the case of an upward flowing jet, the film accelerates as it flows away from impact point, whereas for a downward flowing jet it decelerates. If the jet is directed upward, no force opposes its flow outward the impact zone. In the experimental work of Swedish *et al.* [2], Gilpin [19] and Yen *et al.* [18] the jet was in the upward direction before impinging a solid, that is why the flowing film accelerates, and pool effect, which corresponds to the collapse of the film in the cavity thus filling it, cannot occur.

. These studies used simulant materials, water and ice for Gilpin and Yen *et al.* [18, 19]. In the apparatus used, ablation front position was recorded. They all obtained ablation rates which were independent of time. Powers [9], Saito *et*

al. [7] and Sato *et al.* [20] used materials with properties closer to what could be encountered during a severe accident in a SFR. Powers [9] used stainless steel, iron, alumina impacting a steel structure. Saito *et al.* [7] used molten salt (NaCl) impacting on tin (Sn) and alumina (Al_2O_3) impinging on stainless steel. Sato *et al.* [20] used tin jet impacting onto tin, and stainless steel impacting on stainless steel. Ablation rates were determined by recording the time needed for the jet to break through test plates. Heat transfer coefficient and the associated Nusselt numbers were determined using equation (12). Ablation rate was here assumed constant. The heat transfer coefficient was then computed by balancing heat at the interface. This balance assumes Newton's law and a jump condition on enthalpy.

$$h_{eff}\left(T_{0,j} - T_{f,s}\right) = V_f \rho_s \left[L + C_{p,s}\left(T_{f,s} - T_{0,s}\right)\right] \tag{12}$$

Sato *et al.* [20] determined a scaling law from their experimental work (Eq. (13)). In their experiments, the Reynolds number ranged from 41 000 to 490 000 and the Prandtl number ranged from 0.0095 to 0.20.

$$Nu_f = 0.0152 Re^{0.92} Pr^{0.8} \tag{13}$$

Saito *et al.* [7] and Sato *et al.* [20] reported collapse of the liquid film flowing outward of the cavity for several experiments. It led to the formation of a liquid pool. This effect, named pool effect by Saito *et al.* [7], was linked to a reduction in ablation rate for experiences in which it was identified. In their studies Saito *et al.* [7] and Sato *et al.* [20] excluded experiments exhibiting pool effect from their analysis. Therefore, their scaling laws are only valid before pool effect onset.

. An experimental apparatus named HAnSoLO for Hot AblatioN of a SOlid by a Liquid – Observations, was built in LEMTA by the authors to study the ablation phenomenon using simulant materials. Ablation is simulated using a liquid water jet impacting on transparent ice. The jet is vertical, directed downward.

. Previous work either used jets directed upward or recorded only the average ablation velocity by recording the total time needed to drill through a solid of known thickness. The work presented here give real time ablation results with a jet directed downward. These data can be compared to the studies cited previously. Moreover, some data are given on the pool effect onset. It is a first step to take pool effect into account in future SFRs core-catcher designs.

. The main goal of this work is to gather experimental data, and obtain physical knowledge on ablation phenomenon to improve core-catcher designs so that they can resist to corium even if directly impacted by a coherent free jet of corium. It will help for qualification of numerical codes which are developed for safety analysis of future SFRs. The physical knowledge gathered will also give directions for future developments. Some valuable data can be obtained by the HANSOLO set-up to help to understand the physics underlying the ablation process and further to design the best geometry for the core-catcher which will likely not be a simple wall.

. Study presented here focuses on ablation phenomenology, influence of jet temperature and speed at impact. No fragmentation was taken into account. Influence of the jet diameter is not directly studied and is fixed at 6 mm. The first section is devoted to the description of HAnSoLO experimental installation. It is followed by the presentation of experimental results, which is divided in five parts. This section begins with a summary of experimental conditions and results on ablation velocity and Nusselt number. Then the experimental scaling law computed from experiments obtained in LEMTA is presented. An analysis of the relative depth at pool effect onset follows. The final part before conclusions concentrates on a global phenomenological analysis.

4. Experimental apparatus

. Hot Ablation of a SOlid by a Liquid - Observation (HAnSoLO) installation aimed at studying ablation of transparent ice by a hot water jet. Ablation front

is recorded using high-speed camera. It is the first time, at best of authors knowledge, that such ablation process (i.e. cavity shape formation) is recorded in real time for a downward flowing jet.

. A steady jet at fixed flow rate and controlled temperature impinges the transparent ice block which temperature is close to its melting temperature. A schematic is available in Fig. 4. Table 1 gives the possible experimental conditions for this setup. The conditions that could be encountered in a hypothetical severe accident in a pool-type SFR similar to ASTRID are also given in the table 1. In case of a severe accident in a SFR with formation of corium and relocation of the metallic phase of corium, the Reynolds number of the corium jet at the impact on the core-catcher could be as high as 1 000 000. The Reynolds numbers in HAnSoLO experiments can reach 270 000, which is still one order of magnitude lower. However, the Reynolds numbers are always above 4 000 in HAnSoLO setup. Therefore, the jets produced in HAnSoLO are turbulent [11]. In terms of melting number B, the water / ice experiments are representative of what could be encountered during a severe accident in a SFR. The main difference between the simulating water / ice experiments and the prototypical metal / metal system is the thermal conductivity, which is higher for liquid metals than for water. This affects the Prandtl number value, which is lower than unity for liquid metals and is above unity for water.

. Water is heated in a tank (Fig. 4). An eccentric screw pump ensure a constant flow rate which is recorded thanks to an electromagnetic flowmeter. A controlled three-way valve is positioned before nozzle. It keeps liquid in the loop (back to the tank) until the begin of the run. We let water flowing in this loop for at least 10 min in order to remove air in tubing and bring the pump and pipes at the prescribed temperature. When a stable temperature is reached (i.e. close to the prescribed one), the three-way valve is opened and the run begins.

. Adjustable support allows for tuning of jet drop height. Nozzle-to-plate ratio influences ablation in two ways: (i) jet is accelerated by gravity (Eq. (14))

Figure 4: HAnSoLO experimental facility. TT: Temperature Transmitter; PT: Pressure Transmitter; LT: Level Transmitter; TC: Temperature controller.

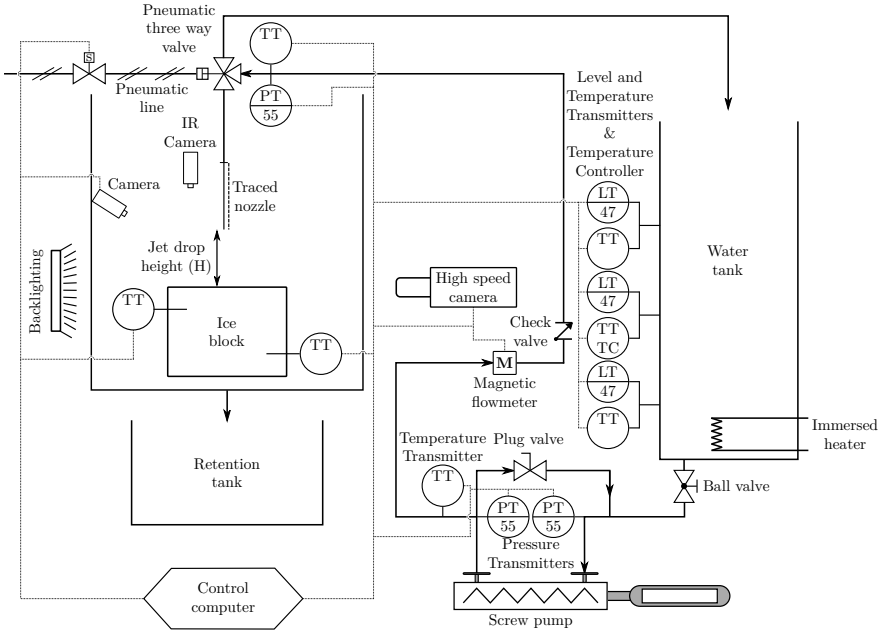

and acceleration increases heat transfer, (ii) the other way is due to the velocity profile within the jet. At nozzle outlet the velocity profile is not uniform. As the jet drops, its velocity profile relaxes [22] but to reach an uniform one, H/d_0 must be greater than 6. Therefore, the drop height was measured for every experiment and maintained above 6 times nozzle inner diameters. [8, 23]. Stevens *et al.* [24] studied the influence of drop height on heat transfer. They noted a weak influence on Nusselt number ($Nu \sim (H/d_0)^{-0.04}$), when $H/d_0 > 6$.

. Nozzle (Fig. 4) is located at the end of the tube passing through the adjustable support. Its length is 50 times nozzle inner diameter to ensure a fully developed turbulent flow at its outlet. A heater is coiled around the nozzle to bring it to prescribed temperature with reduced heat losses. Ice block is fixed by mean of rods inserted inside the block, which are later screwed onto a positioning plate. Two thermocouples are also embedded to control ice temperature.

	HAnSoLO		ASTRID
Value	Minimal	Maximal	Considered
Jet velocity (V_j)	1.0 m/s	10.0 m/s	10.0 m/s
Jet temperature ($T_{0,j}$)	20 ^oC	80 ^oC	1 727 ^oC
Solid temperature ($T_{0,s}$)	0 ^oC		400 ^oC / 1 400 ^oC
Jet diameter (d)	3.0 mm	10.0 mm	80.0 mm
Reynolds number (Re)	4 000	270 000	1 000 000
Prandtl number (Pr)	2.5	7.0	0.13
Melting number (B)	0.25	1.0	0.27 / 0.95

Table 1: Summary of experimental conditions which can be reached in HAnSoLO compared to what could be encountered in a pool-type SFR like ASTRID [21]. Two initial solid temperatures are presented for the solid temperature. The first one corresponds to the case where the core-catcher is at its nominal working temperature (400 ^oC), the second one corresponds to an extreme case where the core-catcher has been brought at its melting temperature by previous interactions.

. To manufacture transparent ice blocks, a mold filled with water is placed in a cooling fluid (brine). To ensure transparency of the blocks gas bubbles must be removed as they form on solid / liquid interface. To do so, water is stirred during the solidification process. As the solidification must be directional, the sides of the molds are thus insulated. The blocks used are 50 cm in length along the optical axis, 25 cm in width and 25 cm in height.

. To ensure safety and prevent water splashes, the runs take place in a chamber. Ablation is recorded using a high-speed camera with back-lighting. The maximum frame rate used with the high-speed camera is 250 Hz. The exposure time was set at 1/2000 s. The uncertainty on the time at which a frame is taken is 0.5 ms. Splattering and run-off are prevented from disturbing the optical axis using protective gears placed on each side of the block. These protective gears change the visualization within the upper part of the block. Cavity cannot be located in this zone. Therefore, we mention this zone as the "blind" zone. This

zone is pictured farther, with the discussion on cavity evolution (Fig. 12). Two other cameras are used, one is an infrared camera and the other one is conventional camera; they are placed inside the chamber, their axis pointing toward the top surface of ice block. The IR camera controls if jet temperature does not vary much during the run, the other one gives an idea of the regime.

5. Results and discussion

5.1. Experimental conditions

. For all the test runs, nozzle's diameter does not change and is equal to 6 mm. It is also important to notice that the influence of the initial temperature of the ice is not studied here. Before each test run, temperature of the ice blocks are controlled and the run cannot begin if their temperature is too low and inhomogeneous. To achieve that, they are thermalised during one hour in the chamber of HAnSoLO which is at room temperature. Thermalisation is deemed achieved when both thermocouples give temperatures above -2 °C . Precision of embedded thermocouples is estimated as 2 °C . We must also precise that ice cracks quickly at jet impact if its temperature is below -5 °C [25].

Initial ice temperature has two consequences on ablation, (i) it induces a delay in ablation start if contact temperature at solid / liquid interface is below jet solidification temperature, ii) it slows ablation rate as the heat first increases the temperature of the ice block before its melting.

. In the study, blocks are close to their melting temperature. Therefore, the contact temperature at solid / liquid interface is above the melting temperature of ice. To assess initial block temperature effect, the Stefan number ($St = C_{p,s}\left(T_{f,s} - T_{0,s}\right)/L$) is computed. This dimensionless number compares sensible heat to latent heat. Using the overestimated value of 5 °C for $(T_{f,s} - T_{0,s})$, St equals to 3.1×10^{-2}. Therefore, the effect of initial ice temperature can be neglected.

. Prescribed jet temperatures of 30°C , 50°C and 70°C above melting point are studied. Uncertainty on temperature is of 2 °C .

. Five different nozzle outlet average velocities are studied: 1 m/s, 2.5 m/s, 5 m/s, 7.5 m/s, 10 m/s. Average velocities are measured thanks to a magnetic flowmeter (Fig. 4). The flow rate is recorded for each experiment. Let us remember that the accuracy of the flowmeter varies with the flow rate.

Uncertainties on velocities are estimated from the accuracy of the flowmeter. As the jet accelerates due to gravity, a direct application of Bernoulli's theorem, and mass conservation, gives Eqs. (14) which are used to determine the new jet characteristics at impact.

$$V_j = \sqrt{V_{0,j}^2 + 2gH} \quad ; \quad d_{imp} = d_0 \left(1 + \frac{2gH}{V_{0,j}^2}\right)^{-1/4} \tag{14}$$

A summary of the experiments done are presented in a phase diagram, Fig. 5 and table 2. The variation of Prandtl number is due to the change in temperature. To compute the uncertainties, the minimum and maximum values of the Prandtl and Reynolds numbers are computed using the uncertainties on the input data [26]. Both Fig. 5 and table 2 show that the experimental Reynolds numbers range from 11 000 to 147 000. Also, the Prandtl number ranges from 2.52 to 5.42. The experimental points are evenly spread in terms of Prandtl number and in Reynolds number.

5.2. Ablation rate and Nusselt number

. Interface location is determined along jet axis during the first ablation regime (i.e. before pool effect). Python 3 and Scikit-Image [27] are used for image processing. First, spatial extent of a pixel is determined and this gives the uncertainty on position of the front. Jet axis and block surface positions are determined visually. To identify and thus locate the cavity, background is removed. Then raw grayscale images are binarized using a threshold on intensity. Pixel intensity now has two values 1 if its intensity is above the threshold and 0 if its intensity is below the threshold. Pixels with 1 as a value are deemed to be part of the cavity. Several methods can be used to determine the threshold. The first is to use a fixed value. To determine this threshold, we tested several

Figure 5: Representation of the experiments in the Prandtl number / Reynolds number domain. The uncertainties are represented for each data point by means of arrows.

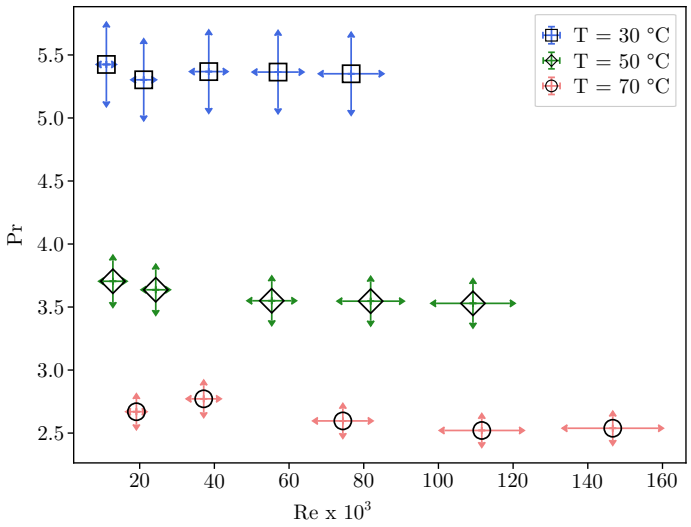

values and chose the one which works the best for most experiments. A value of 30 (out of 256 gray levels) is therefore chosen for all tests. The other methods are Otsu's [28], Li's [29] and sometimes Yen's [30] ones. Artifacts can result in groups of pixels which intensity is above the threshold but are not part of the cavity. Therefore, when artifacts are noticed, they appear as clusters of pixels. They are removed. The minimum number of pixels a cluster needs to have to be kept, was determined for each experiment in order to keep the pixels corresponding to the cavity and removing the ones generated by artifacts. Interface location along jet axis is then obtained by running through the pixels along jet axis from bottom to top and recording the depth at which there is a change in values of pixels from 0 to 1. Sometimes droplets or flow in the optical axis can make noise and disturb the image processing. Corresponding data points are removed when possible by applying the above technique. In the beginning of the run, first data points do not always follow the global trend. As those points are close to the "blind" zone, in which data points are not usable, they are also deleted. Nevertheless, number of removed data points never exceeds 5 %.

Exp. ref.	$T_{0,j}$ °C	$V_{j,imp}$ $m.s^{-1}$	d_{imp} mm	H cm	t_{pe} s	Re_{imp}	Pr	B	We_{imp}
11	30	1.5	5.0	5.8	20.1	11 000	5.42	0.37	185
12	31	2.8	5.8	6.0	31.7	21 000	5.30	0.38	646
13	30	5.1	6.0	6.5	28.8	39 000	5.37	0.38	2 199
14	30	7.6	6.0	6.5	31.6	57 000	5.36	0.38	4 823
15	30	10.2	6.0	6.8	28.7	77 000	5.35	0.38	8 663
21	48	1.2	4.9	4.3	14.9	13 000	3.70	0.60	131
22	49	2.3	5.6	6.0	16.2	24 000	3.64	0.61	456
23	50	5.1	5.9	6.0	14.9	55 000	3.55	0.63	2 274
24	50	7.5	6.0	6.1	15.1	82 000	3.55	0.63	4 963
25	51	10.02	6.0	6.0	14.4	109 000	3.53	0.63	8 769
31	67	1.4	4.8	5.8	8.4	19 000	2.67	0.84	170
32	65	2.75	5.8	5.5	10.9	37 000	2.77	0.81	682
33	69	5.21	5.9	5.0	8.9	74 000	2.60	0.87	2 462
34	71	7.61	6.0	6.0	9.5	112 000	2.52	0.89	5 282
35	71	10.06	6.0	5.0	7.9	147 000	2.54	0.88	9 225

Table 2: Detailed summary of experiments carried out. Exp. ref. is the experiment reference. $T_{0,j}$, $V_{j,imp}$, d_{imp}, Re_{imp}, Pr, B, We_{imp} are jet temperature, velocity, diameter, Reynolds number, Prandtl number, melting number B and Weber number at impact. H is jet drop height. t_{pe} is the time of transition to pool effect. The absolute uncertainties associated to the parameters reported in the table are available in table 4 reported in appendix.

. Due to noise on data points, direct determination of ablation rate is not easy so a regression is performed instead of a direct derivative. All previous authors assumed a constant ablation rate [10, 8, 7, 20, 15]. Swedish *et al.* [2] model predicts a constant ablation rate provided that jet temperature, speed and diameter do not vary at impact. For jet temperature, IR measurements showed that the jet did not loose heat while falling from the nozzle to the solid surface. Variations of jet velocity and diameter are due to gravity acceleration

according to Eq. (14). We assumed that the velocity at impact does not vary during the film regime[4]. Swedish *et al.* [2] stated that the ablation rate is constant and showed experimental data to back up their claim. Finally, our measurements show that it is indeed constant before the onset of pool-effect.

Therefore, we assume a constant ablation rate, and data before pool effect are regressed using a linear model with nonzero value at origin. This nonzero value or "depth at time origin" is kept due to uncertainties on ice surface location. Let us emphasize that time zero surface location does not influence ablation rate. Then residuals are plotted as a function of time and compared to the uncertainty on position. For any analysis, no significant global trend in residuals is observed. Determination coefficient R^2 is always above 0.99.

. An example of results is reported in Fig. 6, the residuals and the uncertainty on position are also reported on the same figure. The residuals show an increase at beginning and decrease at the end of linear regression. The increase can be explained by a weak ice curvature at top side, while the decrease can stem from early effect of transition to pool effect. Ablation rates for all tests are summarized in table 3. Heat transfer coefficient is computed from ablation rate (V_f) using Eq. (10).

. Experimental values are reported in table 3 along with results of previous scaling laws: Nu_1 (Eq. (15)) is obtained using Eqs. (11), (3) and (4) as recommended by Swedish *et al.* [2], Nu_2 is calculated using Sato *et al.* [20] scaling law (Eq. (13)).

$$Nu_1 = 0.5077 \frac{ln(1+B)}{B} Re^{0.523} Pr^{0.33} \tag{15}$$

[4]In fact the jet accelerates as the cavity digs deeper into the solid. However, this acceleration can be assessed using the measurement of depth of transition to pool effect presented farther in section 5.4 using equation (14). An average increase in velocity of only 4 % was calculated with a standard deviation of 4 %. This confirms our hypothesis to neglect this effect.

Figure 6: From top to bottom : evolution of depth as a function of time for test 23 over the full data range, evolution of depth as a function of time for test 23 before pool effect and regression residuals. Blue crosses are data points. Best fit before pool effect is represented by a black line. The time of pool effect transition is pictured as a discontinued vertical red line. Uncertainty on position is pictured as horizontal dashed black lines with the residuals.

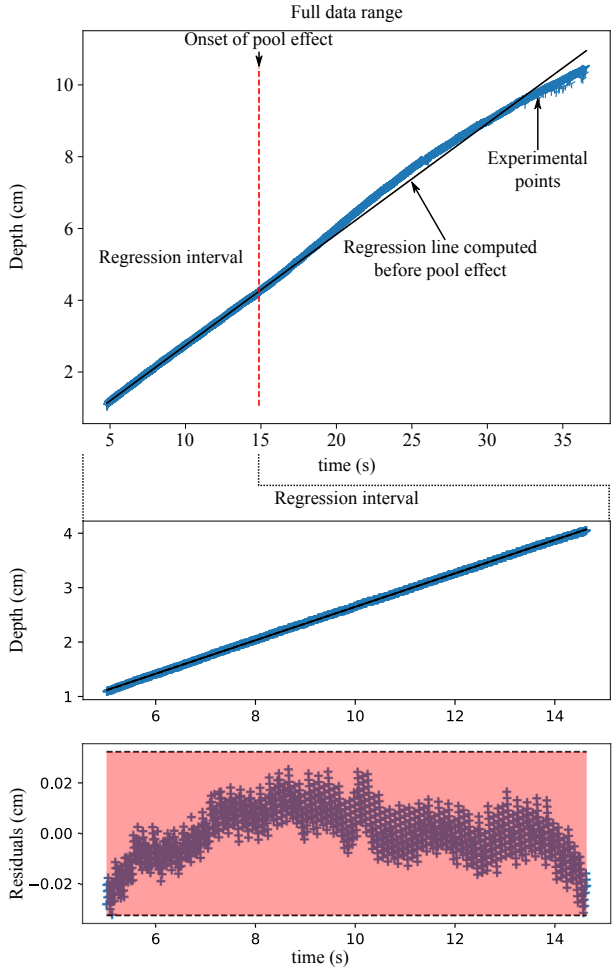

Ablation rates predicted using Swedish *et al.* [2] approach with two immiscible fluid layers are reported in the table as $V_{f,si}$. For the calculations, the temperature dependency of fluid properties is taken into account. To do so, first the layer of melted solid is assumed at melting temperature of the solid and the fluid in the boundary layer present beneath the jet is assumed at a temperature

equal to the initial jet temperature. An ablation velocity is then computed using Swedish *et al.* [2] model – *cf.* equations (5) to (8). The interface temperature is computed using equation (9). It is then possible to give a better estimate of the temperature at which the properties should be computed. This temperature is $T = \frac{1}{2}(T_i + T_{f,s})$ for the layer of fluid coming from the melting of the solid and $T' = \frac{1}{2}(T_i + T_{0,j})$ for the boundary layer of fluid coming from the jet. A new estimate of the ablation velocity is then computed using equations (5) to (8). The procedure is carried out until the average relative difference ϵ between two steps $N-1$ and N is below 10^{-8}.

$$\epsilon = 2\left|\frac{V_{f,N} - V_{f,N-1}}{V_{f,N} + V_{f,N-1}}\right|$$

The film thickness at the end of the stagnation zone can be determined using a mass balance assuming the fluid as inviscid. The end of the stagnation zone is given by Liu *et al.* [31] – Eq. (16). The thickness of the liquid film is, for our experiment of 0.95 mm.

$$\frac{2r}{d} = 1.574 \tag{16}$$

The thickness of the layer of fluid coming from the melting of the solid can be estimated from Swedish *et al.* [2] method. For instance, for experiment referenced 23 this thickness is of $1.2 \cdot 10^{-2}$ mm. Therefore, it is 79 times smaller than the film thickness. It may explain why the approximate model of Swedish *et al.* [2] works in our case.

Swedish *et al.* [2] method with two fluid layers is close to our experimental results but is always lower. This can be noticed on the parity plot available in figure 7. Whereas the approach using a correction (Eqs. (3) & (11)) gives results close to the experimental ones. This can be observed in the parity plot available in figure 8. However, one can note a trend in the difference between results obtained using this method and the experimental results presented here as it overestimates the Nusselt number at low velocity and underestimate it at high velocity. Nevertheless, these comparisons show that we can be quite

confident in the accuracy of these methods to determine the ablation rates when the boundary layers in the stagnation zones are not disturbed by turbulence in the jet.

Figure 7: Parity plot showing the variation of the ablation speed computed using Swedish *et al.* [2] approach $V_{f,si}$ with respect to the experimental ablation velocity $V_{f,exp}$. The bisector is also pictured as a solid black line.

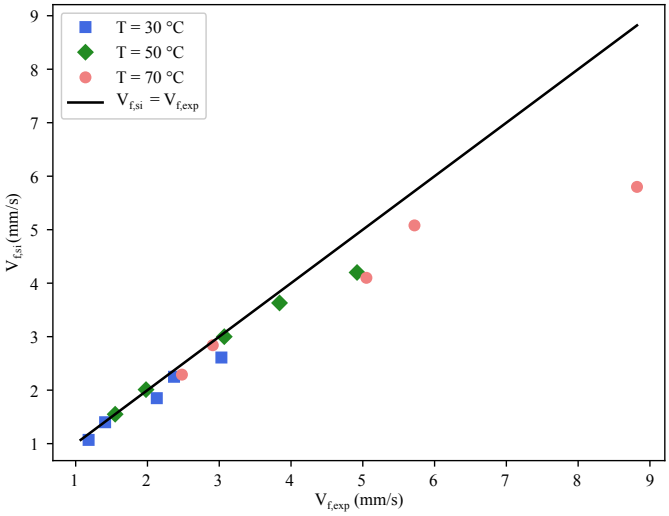

. Nusselt number predicted using the scaling law of Sato *et al.* [20] are far from the ones we obtained experimentally. This scaling law which is a reference in nuclear design for metal jet impacting on metallic solid does not describe the ablation of ice by a water jet well. This is certainly due to the difference in Prandtl number for liquid metals ($Pr < 1$) and water ($Pr > 1$). It can also be induced by the difference in Reynolds number as the maximum Reynolds number in the study of Sato *et al.* [20] is twice the maximum Reynolds number achieved for the experiments reported here with HAnSoLO.

Figure 8: Parity plot showing the variation of the Nusselt number Nu_1 (Eq. (15)) as a function of the Nusselt number obtained experimentally Nu_{eff}. The bisector is also pictured as a solid black line.

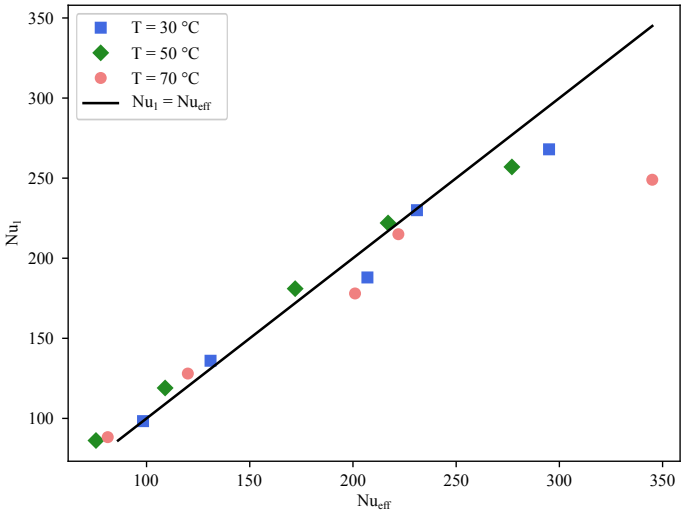

Exp. ref.	$V_{f,exp}$ $m.s^{-1}$	$V_{f,si}$ $m.s^{-1}$	h_{eff} $W.m^{-2}.K^{-1}$	Nu_{eff}	Nu_1	Nu_2
11	1.18×10^{-3}	1.07×10^{-3}	1.21×10^{4}	98.3	98.3	309
12	1.41×10^{-3}	1.40×10^{-3}	1.41×10^{4}	131	136	548
13	2.13×10^{-3}	1.85×10^{-3}	2.16×10^{4}	207	188	965
14	2.37×10^{-3}	2.25×10^{-3}	2.39×10^{4}	231	230	1 384
15	3.03×10^{-3}	2.61×10^{-3}	3.05×10^{4}	295	268	1 812
21	1.55×10^{-3}	1.55×10^{-3}	9.90×10^{3}	75.5	86.2	260
22	1.98×10^{-3}	2.01×10^{-3}	1.24×10^{4}	109	119	463
23	3.07×10^{-3}	3.00×10^{-3}	1.87×10^{4}	172	181	968
24	3.84×10^{-3}	3.63×10^{-3}	2.34×10^{4}	217	222	1 386
25	4.92×10^{-3}	4.20×10^{-3}	2.98×10^{4}	277	257	1 800
31	2.48×10^{-3}	2.29×10^{-3}	1.13×10^{4}	81.2	88.3	290
32	2.91×10^{-3}	2.84×10^{-3}	1.37×10^{4}	120	128	550
33	5.05×10^{-3}	4.10×10^{-3}	2.24×10^{4}	201	178	989
34	5.72×10^{-3}	5.08×10^{-3}	2.46×10^{4}	222	215	1 403
35	8.82×10^{-3}	5.80×10^{-3}	3.82×10^{4}	345	249	1 814

Table 3: Ablation results before pool effect. Exp. ref. is the experiment reference. $V_{f,exp}$: ablation speed determined experimentally. $V_{f,si}$: ablation speed determined using Swedish *et al.* two layers immiscible layers method. h_{eff}: effective heat transfer coefficient. Nu_{eff}: experimental Nusselt number. Nu_1: Nusselt number calculated using Eq. (15). Nu_2: Nusselt number calculated using scaling law (13).

5.3. Scaling law in the flowing film regime

. From our experimental results, an experimental scaling law has been determined. It will be useful for operational design and can also help physical interpretation. In forced convection flow, the theory [17, 32] shows that Nusselt, Reynolds and Prandtl numbers are linked by the following Eq. (17). The change in Prandtl number in our experiment is due to the change in water temperature. It is limited to the interval $[2.52 - 5.42]$, which is less than a decade. It would therefore be difficult to determine m from our experimental data. We therefore assumed a value of $m = \frac{1}{3}$ for the exponent over the Prandtl number, which is valid for $Pr > 1$ and is in agreement with theoretical predictions.

$$Nu = KRe^{n}Pr^{m} \tag{17}$$

We chose to include the effect of melting by using the correction given in Eq. (3). The general form of the scaling law sought is therefore given by Eq. (18).

$$Nu\frac{B}{ln(1+B)} = KRe^{n}Pr^{\frac{1}{3}} \tag{18}$$

. Figure 9 shows the variation of $Nu\frac{B}{ln(1+B)}Pr^{-\frac{1}{3}}$ as a function of the Reynolds number in logarithmic scale. The two quantities are proportional, meaning that our data can be represented by an equation as Eq. (18).

. To determine, K and n, natural log of Eq. (18) is used (Eq. (19)). Multilinear regression is then computed with a special care to regression significance. Therefore, in addition to the statistical determination coefficient (R^2), a Student-t test [33] is used to obtain 95 % the confidence interval on n. For K, limits of its uncertainty interval are taken as the exponential of uncertainty interval limits on $ln\,(K)$. This can be done as the exponential is an increasing function.

$$ln\left(Nu\frac{B}{ln(1+B)}Pr^{-\frac{1}{3}}\right) = ln\,(K) + n.ln\,(Re) \tag{19}$$

Figure 9: Evolution of $Nu\frac{B}{ln(1+B)}Pr^{-\frac{1}{3}}$ as a function of the Reynolds number Re in logarithmic scale for the experiments used for regression (tables 3 & 5). The uncertainties are pictures by blue arrows for each data point.

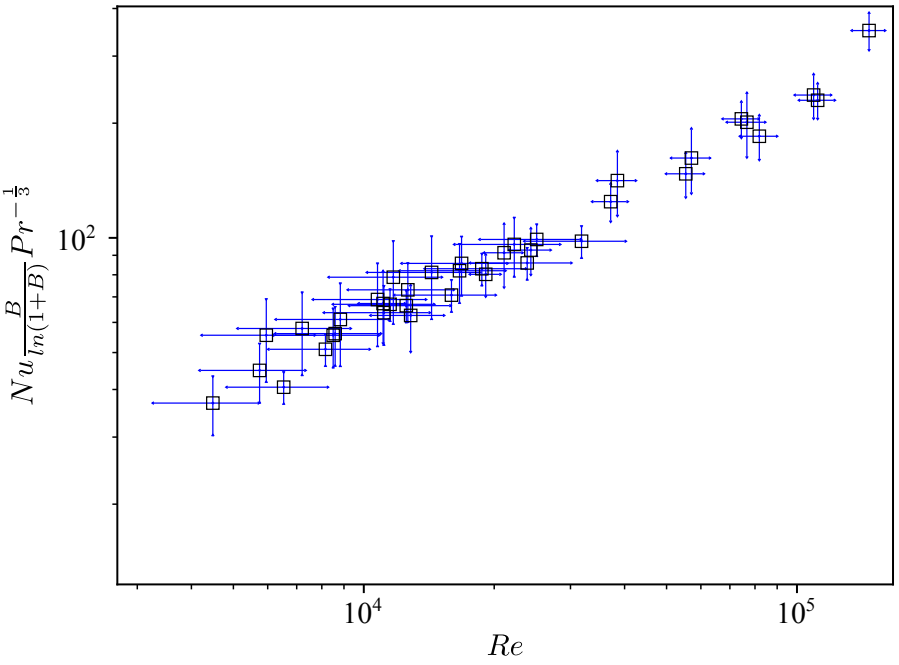

. Analysis was previously done using other data obtained at the laboratory with a smaller scale experiment and smaller nozzle diameters (summary of these data is available in appendix, table 5). Cavity dynamics are the same in the present and former experiments. Therefore, to extent data range and to improve regression precision, these data are also used. Scaling law (20) is obtained. Validity intervals, confidence interval as well as determination coefficients are gathered below Eq. (20).

$$Nu_f = 0.33\frac{ln(1+B)}{B}Re^{0.57}Pr^{1/3} \tag{20}$$

With:

$$Re \in [4\ 500 - 147\ 000] \quad ; \quad Pr \in [2.52 - 5.42]$$

$$K = 0.33 \pm 0.11 \quad ; \quad n = 0.57 \pm 0.03 \quad ; \quad R^2 = 0.97$$

. Reynolds number exponent is close to the theoretical value for laminar flow [17], namely $\frac{1}{2}$. The parity plot for the regression is available in figure 10. No global trend can be noticed in data points deviation from the bisector. The scaling law derived (Eq. (20)) describes our data with a maximum uncertainty of around 20 %.

Figure 10: Parity plot of the value of $Nu\frac{B}{ln(1+B)}Pr^{-\frac{1}{3}}$ computed using the scaling derived here (Eq. (20)) as a function of value computed using experimental data. This bisector is also shown along with the area corresponding to 10 % and 20 % of deviation from the bisector.

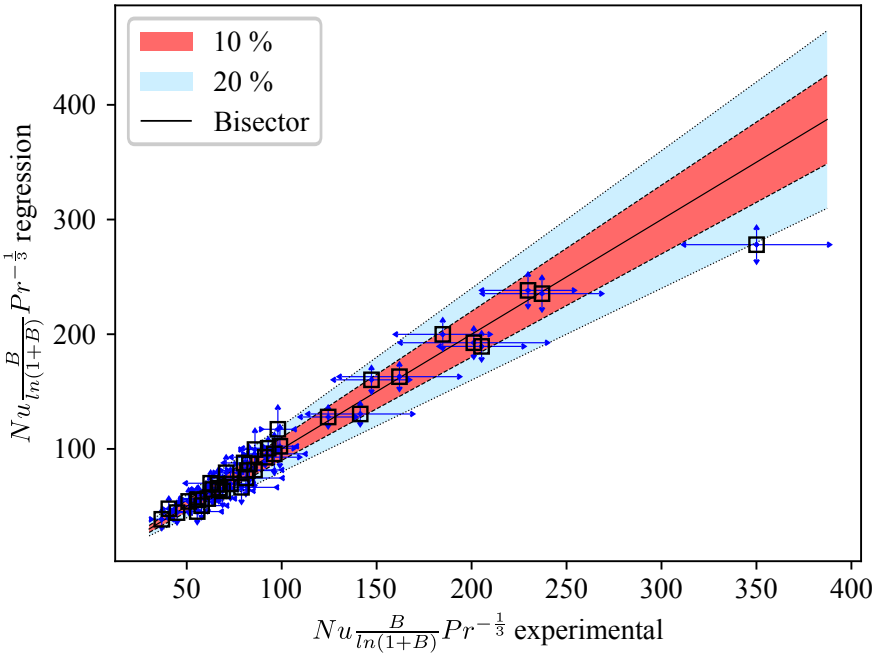

5.4. Pool effect

. Figure 11 shows relative cavity depth $Z^* = z/d$ at onset of pool effect regime, as a function of jet velocity for the experimental runs performed. Markers shapes and colors correspond to jet prescribed temperature. We identified the time of pool effect onset to the time at which the cavity becomes filled with liquid. From their experimental results, Saito *et al.* [7] stated, that pool effect can appear for $Z^* \geqslant 4$. This finding is globally confirmed with our experimental results (except

for test 31). However, this criterion is not enough to predict accurately the onset of pool effect regime. The higher the jet velocity the higher the difference between experiments and Saito's *et al.* [7] criterion, with an experimental value more than three times greater than the one estimated by Saito's *et al.* [7] (for the higher velocities tested). Data gathered in this study show that Z^* globally increases with jet velocity reaching a value as high as 14.

We strongly believe that the transition to pool effect must be linked to the equilibrium of the outgoing radial current which must be balanced by gravity effects, this will need more in depth analytical study which is not developed here.

. Saito *et al.* [7] described the pool effect as a phenomenon reducing the ablation rate. However, we have found that it is not always the case. In the top graph of figure 6, the evolution of cavity depth at impact point is reported for the experiment 23. The experimental points lay above the line representing the regression of the depth as a function of time before the onset of pool effect, meaning that the ablation rate initially increase before decreasing later. This behavior has never been reported, to the best of our knowledge. We observed the occurrence of pool effect with a visible camera while previous authors used more integral data to detect pool effect transition; this could explain this difference in noticed behavior.

Figure 11: Dimensionless depth at onset of pool effect (Z^*) as a function of jet velocity. Marker shape and color indicate the prescribed temperature.

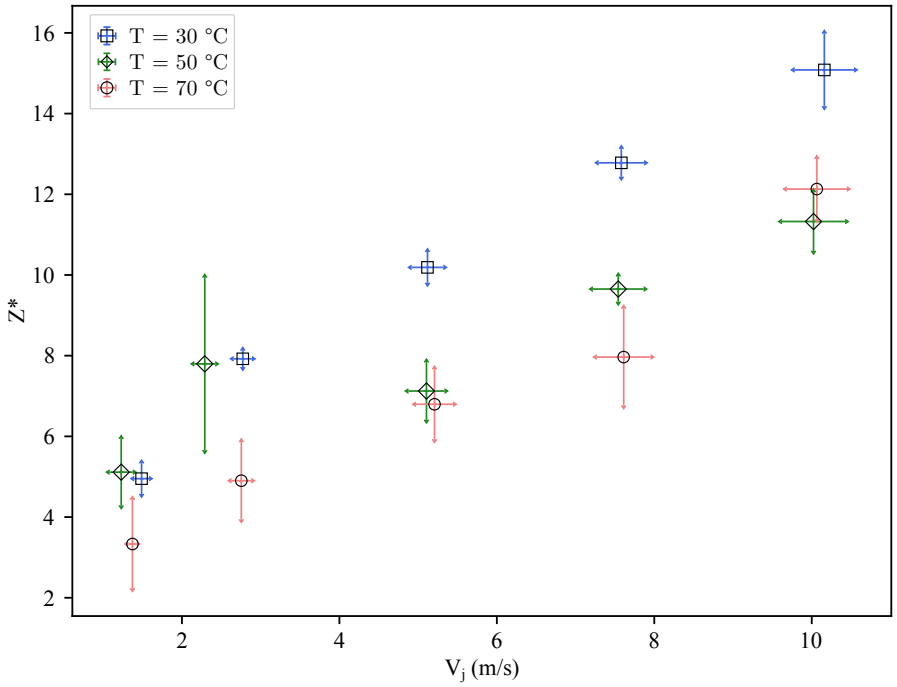

5.5. Ablation phenomenology

. Global phenomenological understanding is the basis of a future physical modelling of the ablation process. Figure 12 gives an example (test 23) of cavity shape evolution as ablation is in progress. Figures 14, 15 and 16 show photographs of cavities for each test reported in table 2. A dimensionless time $t^* = t/t_{PE}$ is defined to help comparison. Cavities are reported for $t^* = 0.5$, $t^* = 1$ and $t^* = 1.5$.

. Figure 12 gives an illustration of the sequence but it is important to notice that the very beginning of each test is never observed by the high speed camera as a "blind" zone exists and covers a thickness of around 1 *cm*. It is due to some protection devices and to the local curvature of ice which melts faster at the edges (let us remind that the optical path from lighting to camera crosses these

Figure 12: Cavity shape evolution, test 23. With main geometric characteristic points noted. A: Impact point. B,B': End of stagnation zone. C,C': First inflexion point. D,D': Second inflexion point. E,E': Cavity end. The "blind" zone is highlighted in the image corresponding to $t = 0\ s$.

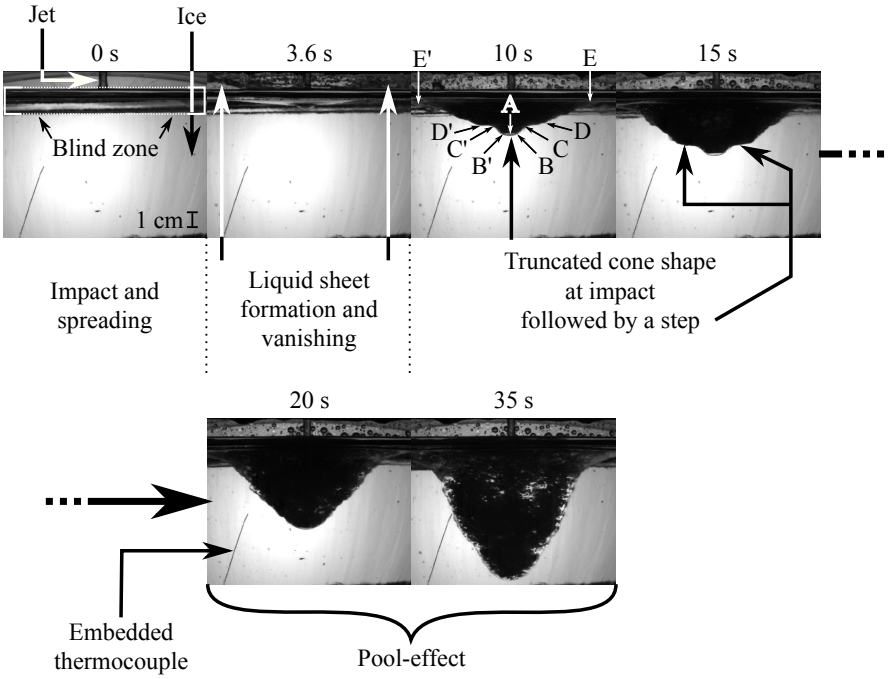

different diopters). Before pool effect, jet spreads as a film and cavity shape seems similar, which indicates that the heat transfer is not time dependent in the film regime, even outside the stagnation zone. Important points are identified for a better understanding and description in Fig. 12 (at $t = 10\ s$). Around the impact point A, between B' and B, cavity appears flat. It implies a constant ablation rate on this surface. This is expected in the stagnation zone, in which the boundary layer is of constant thickness. Its radial extent was determined theoretically by Liu *et al.* [31]. They obtained Eq. (16). Liu *et al.* [31] indicated that this equation was obtained by computing the radial distance at which the thickness of the growing boundary layer outside the stagnation zone is equal to the boundary layer thickness within the stagnation zone. Note

that distance B'B equals $2r$ and slightly exceeds jet diameter. Stagnation zone limits computed using Eq. (16) are pictured on Figs. 14, 15 and 16 with arrows on cavities images before pool effect. It gives a good first estimate of the radial extent of the stagnation zone. For tests 25, 34 and 35 (higher temperatures and jet velocities), it does not apparently match. However, actual stagnation zone mays be hidden in these experiments.

. A roughly conical shape follows stagnation zone between B and a first inflexion point C. Straight cavity slope indicates a constant ablation speed, but lower than in stagnation zone. The plateau between C and D, as well as the inflexion point in D, is not always observed. Visual inspection during test run reveals us that a torus is located within the flat zone between C and D, as shown in Fig. 13. It can explain why this zone appears to change from one test to another, back-lighting giving a projection of the cavity. In this case, point C may not be an actual inflexion point on the cavity; it is the projection of point D on the lower part of the cavity. Sato *et al.* [20] reported several post-test cross sections. The one reported for stainless steel and a thickness of 50 mm shows a cavity quite similar to test 23 before pool effect with a torus. In some experiments, no step is observed (*cf.* test 14 Fig. 14). From point D to E, cavity joins block's top surface following a straight line. End of cavity changes at pool effect onset ($t^* = 1$) due to some instability which begins outside the cavity before water falls inside and fills it.

. Tests 25, 34 and 35 seem to have a different behavior. Let us recall that between impact zone and upper cavity zones, a flat transition is the signature of the presence of a toroidal shape. Distance between points B and C in different cavities (*cf.* figures 14, 15 and 16) decreases as jet speed increases. This, in addition to the fact that no major cavity changes are observed at end of stagnation zone determined by Liu *et al.* (*cf.* Eq. (16)), indicates that the actual shape may be described as a "W" shape but hidden by the back-lighting projection.

Figure 13: Schematic description of the torus (vertical stripes) that may form during ablation and the zone it hides (horizontal stripes). Points of interests identified in Fig. 12 are marked.

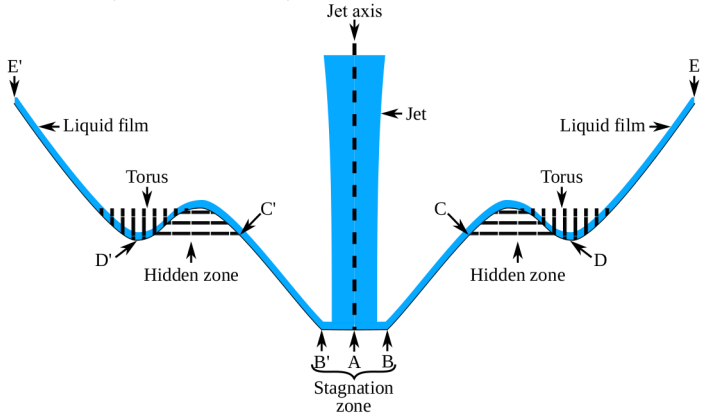

. During pool effect, the cavity shape and dynamics experience a very different evolution implying a change in heat transfer. If a plateau is present before pool effect, then it disappears. Also, overall cavity radius barely changes while cavity depth increases.

. Remind that experiments are carried out in air with a nozzle length to diameter ratio of 50. Some gas entrainment is observed for all tests in pool effect regime. However, for tests 11, 21 and 31, air is not entrained continuously. Maximal jet velocity for these tests is 1.5 $m.s^{-1}$. Minimal jet velocity for tests with continuous air entrainment is 2.3 $m.s^{-1}$. Therefore, in present configuration, the minimal jet velocity to entrain air lies between 1.5 $m.s^{-1}$ and 2.3 $m.s^{-1}$.

. For jets issued from nozzles with length to diameter ratio of over 50 and a diameter of 1.78 mm, Biń [22] reports a minimum entrainment velocity between 1.2 $m.s^{-1}$ and 2.4 $m.s^{-1}$. In his study, Biń presented two criteria for the minimum entrainment velocity (V_e), at low turbulence intensity ($< 3\%$).

. The first is a criterion on jet Weber number (Eq. (21)). Continuous air entrainment occurs for jets with Weber number above this value. It is coherent with our observations (*cf.* table 2) even if this criterion is deemed valid for

nozzles with length over diameter ratio lower than 8.

$$We_j = 400 \tag{21}$$

. The second criterion gives the minimum entrainment velocity (Eq. (22)) and is valid for nozzles with length to width ratio lower than 3. Furthermore, jets are recommended to have a diameter greater than 7 mm.

$$V_e = 1.4\,(H/d_0)^{0.164} \tag{22}$$

. Applying this criterion, we obtain minimum entrainment velocity in the range $\left[1.9\ m.s^{-1}; 2.0\ m.s^{-1}\right]$. It is consistent with our results and a good estimate of the minimum entrainment velocity can be obtained using these two equations. Biń's analysis [34] demonstrates that jet drop height, which is not important for heat transfer before pool effect, is important for gas entrainment. But we do not study the influence of this parameter in the present paper even if we suspect that it has a significant impact on the heat transfer during pool effect. It is also interesting to notice that the two criteria given by Biń [34] give good results in our case even if jet is confined due to the cavity shape.

Figure 14: Cavity shape for tests 11 to 15, at $t^* = 0.5$, $t^* = 1$ and $t^* = 1.5$. Arrows on pictures before pool effect indicate stagnation zone limits calculated with Eq. (16). Scale is the same within a row and is pictured by a black line equal to 1 cm on first image of each row. It may change between rows.

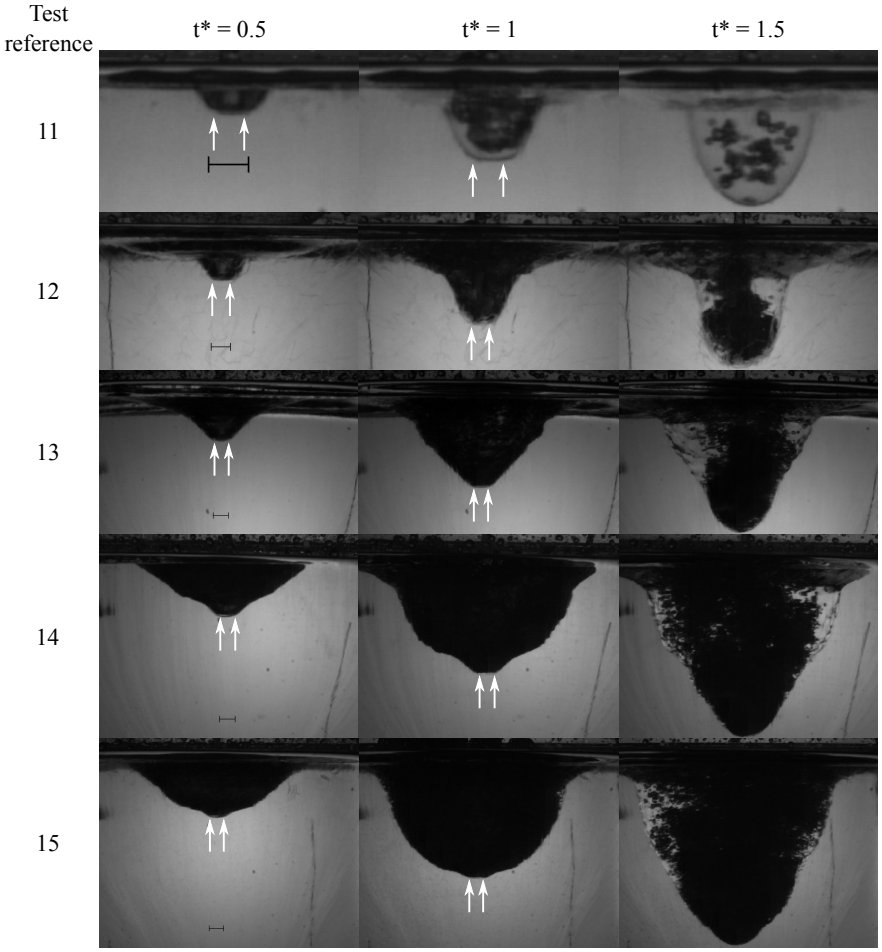

Figure 15: Cavity shape for tests 21 to 25, at $t^* = 0.5$, $t^* = 1$ and $t^* = 1.5$. Arrows on pictures before pool effect indicate stagnation zone limits calculated with Eq. (16). Scale is the same within a row and is pictured by a black line equal to 1 cm on first image of each row. It may change between rows.

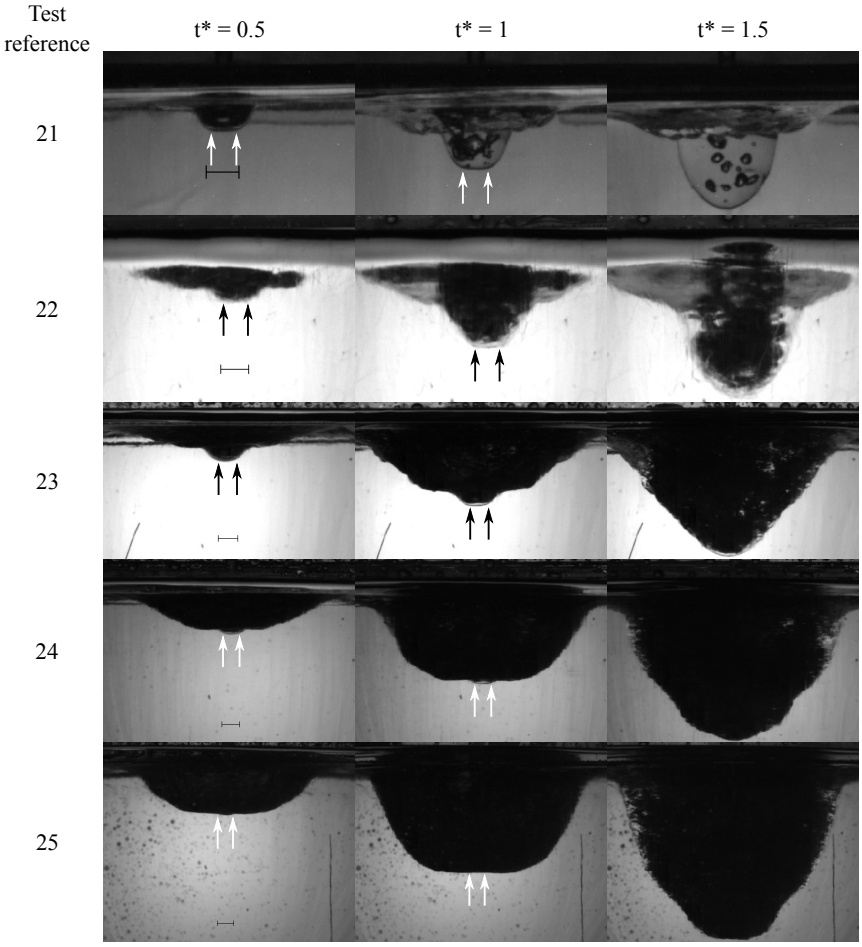

Figure 16: Cavity shape for tests 31 to 35, at $t^* = 0.5$, $t^* = 1$ and $t^* = 1.5$. Arrows on pictures before pool effect indicate stagnation zone limits calculated with Eq. (16). Scale is the same within a row and is pictured by a black line equal to 1 cm on first image of each row. It may change between rows.

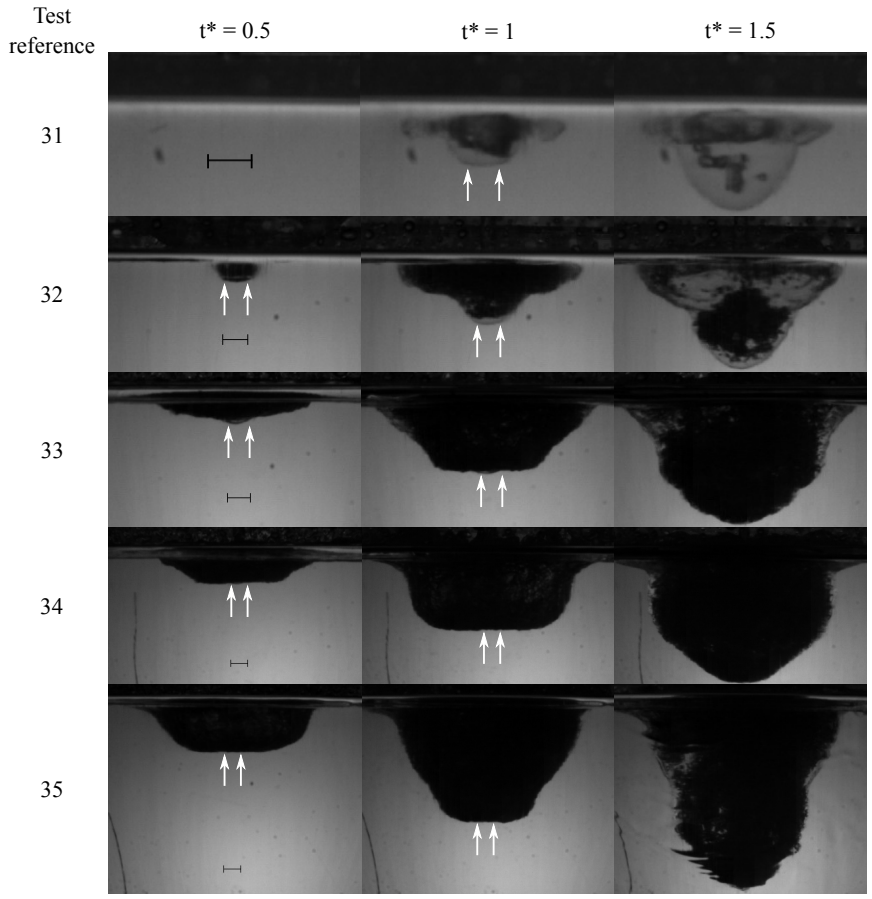

6. Conclusions

. A new experimental setup was built in LEMTA to study water jet ablation of a solid block of transparent ice. It allows for the visualization of ablation in real-time using water and transparent ice. Two main regimes were observed. They were previously reported but it is the first time to the best of author's knowledge that the whole dynamics could be directly observed. The first regime is a film flowing regime which dynamics is similar to that of a jet spreading on a concave surface while the second one, namely the "pool effect", occurs when the spreading film cannot exit the cavity and thus fills it.

. From the analysis of the cavity formation and especially the location of the bottom part of the cavity, we were able to estimate the heat transfer in the stagnation zone of the jet. The obtained experimental results are summarized in table 3. They show a quite good agreement with Swedish *et al.* [2] (see table 3). Nevertheless, a new scaling law has been proposed, for the film regime, which better fit all the experimental data. Previous works [2, 7, 20, 15] found a constant ablation speed during the first regime, that is confirmed by measuring the position of the bottom point of the cavity and then estimating the melting velocity. The scaling law assumes a laminar flow at impact even if the jet is turbulent. Hence, turbulence must be vanished by the pressure of the jet in the stagnation zone.

. We have noted that just after the transition to pool effect the ablation velocity can slightly increase. This phenomenon, which has never been reported, as best of our knowledge, should be further investigated.

. Additionally, we analyzed the onset of pool effect by measuring the ratio Z^*. It starts from around 4 but can go to values up to 11-14, for the highest velocity tested. The condition controlling the transition to pool effect must be better understood as well as heat transfer in this regime. Again, it needs additional analysis to better understand the heat transfer. What we observed, is that, depending on the jet Weber number, some air can be trapped in the pool. Air

entrainment may influence flow dynamics and thus transfers during pool effect and should be further studied.

. Finally, the database which has been gathered during this work can be useful for CFD tools as we captured all the dynamic of the cavity formation. This will be done in further work.

7. Acknowledgments

The research carried in the frame of the ESFR-SMART project leading to some part of results has received funding from the Euratom research and training program 2014-2018 under grant agreement No 754501.

Data on the smaller scale experiment were obtained during the internship of Célien Zacharie, Reda Zaccharia, Théo Michel and Séléna Audhasse.

References

[1] P. Mouchet, M. Roustan, Caractéristiques et propriétés des eaux eau pure, eaux naturelles, Techniques de l'ingénieur Eau : propriétés, qualité, valeurs d'usage base documentaire : TIB506DUO. (ref. article : w110), fre. arXiv:basedocumentaire:TIB506DUO.
URL https://www.techniques-ingenieur.fr/base-documentaire/environnement-securite-th5/eau-proprietes-qualite-valeurs-d-usage-42506210/caracteristiques-et-proprietes-des-eaux-w110/

[2] M. J. Swedish, M. Epstein, J. H. Linehan, G. A. Lambert, G. M. Hauser, L. J. Stachyra, Surface ablation in the impingement region of a liquid jet, AIChE Journal 25 (4) (1979) 630–638. arXiv:https://aiche.onlinelibrary.wiley.com/doi/pdf/10.1002/aic.690250409, doi:10.1002/aic.690250409.

URL https://aiche.onlinelibrary.wiley.com/doi/abs/10.1002/aic.690250409

[3] F. Gauché, Generation iv reactors and the astrid prototype: Lessons from the fukushima accident, Comptes Rendus Physique 13 (4) (2012) 365 – 371, science of nuclear safety post-Fukushima. doi:https://doi.org/10.1016/j.crhy.2012.03.004.
URL http://www.sciencedirect.com/science/article/pii/S1631070512000369

[4] A. Zaetta, Why Fast Neutron Reactors (FRs) ?, in: Sodium-Cooled Nuclear Reactors, cea saclay et groupe moniteur (Éditions du moniteur) Edition, F. Gauché, Paris, 2016, pp. 11–16.

[5] Reactor Harmonization Group RHWG, Safety of new NPP designs, Tech. rep., Western European Nuclear Regulators Association (Mar. 2013).
URL http://www.wenra.org/media/filer_public/2013/08/23/rhwg_safety_of_new_npp_designs.pdf

[6] F. Bertrand, N. Marie, A. Bachrata, V. Brun-Magaud, J. Droin, X. Manchon, K. Herbreteau, B. Farges, B. Carluec, S. Poumerouly, D. Lemasson, Status of severe accident studies at the end of the conceptual design of astrid: Feedback on mitigation features, Nuclear Engineering and Design 326 (2018) 55 – 64. doi:https://doi.org/10.1016/j.nucengdes.2017.10.019.
URL http://www.sciencedirect.com/science/article/pii/S0029549317304983

[7] M. Saito, K. Sato, A. Furutani, M. Isozaki, S. Imahori, Y. Hattori, Melting attack of solid plates by a high temperature liquid jet — effect of crust formation, Nuclear Engineering and Design 121 (1) (1990) 11 – 23. doi:https://doi.org/10.1016/0029-5493(90)90003-G.
URL http://www.sciencedirect.com/science/article/pii/002954939090003G

[8] M. Epstein, M. J. Swedish, J. H. Linehan, G. A. Lambert, G. M. Hauser, L. J. Stachyra, Simultaneous melting and freezing in the impingement region of a liquid jet, AIChE Journal 26 (5) (1980) 743–751. arXiv:https://aiche.onlinelibrary.wiley.com/doi/pdf/10.1002/aic.690260507, doi:10.1002/aic.690260507.
URL https://aiche.onlinelibrary.wiley.com/doi/abs/10.1002/aic.690260507

[9] D. A. Powers, Erosion of steel structures by high-temperature melts, Nuclear Science and Engineering 88 (3) (1984) 357–366. arXiv:https://doi.org/10.13182/NSE84-A18589, doi:10.13182/NSE84-A18589.
URL https://doi.org/10.13182/NSE84-A18589

[10] L. Roberts, On the melting of a semi-infinite body of ice placed in a hot stream of air, Journal of Fluid Mechanics 4 (5) (1958) 505–528. doi:10.1017/S002211205800063X.

[11] J. H. V. Lienhard, Heat Tansfer by Impingement of Circular Free-Surface Liquid Jets, in: S. C. Mishra, B. V. S. S. S. Prasad, S. V. Garimella, I. S. Heat, M. Transfer, A. S. of Mechanical Engineers (Eds.), Heat and mass transfer 2006 : proceedings of the 18th National & 7th ISHMT-ASME Heat and Mass Transfer Conference, New Delhi : Tata McGraw-Hill Pub. Co., ©2006., 2006.

[12] M. Esptein, The effect of melting on heat transfer to submerged bodies, Letters in Heat and Mass Transfer 2 (2) (1975) 97 – 103. doi:https://doi.org/10.1016/0094-4548(75)90047-8.
URL http://www.sciencedirect.com/science/article/pii/0094454875900478

[13] C. Tien, Y.-C. Yen, The Effect of Melting on Forced Convection Heat Transfer, Journal of Applied Meteorology 4 (4) (1965) 523–527.
URL https://www.jstor.org/stable/26172936

[14] O. M. Griffin, Heat, Mass, and Momentum Transfer During the Melting of Glacial Ice in Sea Water, Journal of Heat Transfer 95 (3) (1973) 317–323. arXiv:https://asmedigitalcollection.asme.org/heattransfer/article-pdf/95/3/317/5663482/317_1.pdf, doi:10.1115/1.3450058.
URL https://doi.org/10.1115/1.3450058

[15] A. Furutani, S. Imahori, K. Sato, M. Saito, Erosion behavior of a solid plate by a liquid jet - effect of molten layer, Nuclear Engineering and Design 132 (2) (1991) 153 – 169. doi:https://doi.org/10.1016/0029-5493(91)90263-H.
URL http://www.sciencedirect.com/science/article/pii/002954939190263H

[16] S. Sitharamayya, K. S. Raju, Heat transfer between an axisymmetric jet and a plate held normal to the flow, The Canadian Journal of Chemical Engineering 47 (4) (1969) 365–368. arXiv:https://onlinelibrary.wiley.com/doi/pdf/10.1002/cjce.5450470412, doi:10.1002/cjce.5450470412.
URL https://onlinelibrary.wiley.com/doi/abs/10.1002/cjce.5450470412

[17] H. Schlichting, J. Kestin, Boundary-layer theory, 7th Edition, McGraw-Hill series in mechanical engineering, McGraw-Hill, 1979.

[18] Y.-C. Yen, Z. Anthony, Melting heat transfer with water jet, International Journal of Heat and Mass Transfer 16 (1) (1973) 219 – 223. doi:https://doi.org/10.1016/0017-9310(73)90265-2.
URL http://www.sciencedirect.com/science/article/pii/0017931073902652

[19] R. R. Gilpin, The ablation of ice by a water jet, Transactions of the Canadian Society for Mechanical Engineering 2 (2) (1973) 91 – 96. doi:https://doi.org/10.1139/tcsme-1973-0014.

URL https://www.nrcresearchpress.com/doi/pdf/10.1139/tcsme-1973-0014

[20] K. Sato, A. Furutani, M. Saito, M. Isozaki, K. Suganuma, S. Imahori, Melting attack of solid plates by a high-temperature liquid jet [ii] — erosion behavior by a molten metal jet, Nuclear Engineering and Design 132 (2) (1991) 171 – 186. doi:https://doi.org/10.1016/0029-5493(91)90264-I.
URL http://www.sciencedirect.com/science/article/pii/002954939190264I

[21] F. Bertrand, Proposal for conservatism relaxation related to the core catcher thermal erosion assessment, memo DER/SESI (pour JAEA), CEA/DER/SESI (2017).

[22] A. Biń, Minimum air entrainment velocity of vertical plunging liquid jets, Chemical Engineering Science 43 (2) (1988) 379 – 389. doi:https://doi.org/10.1016/0009-2509(88)85051-6.
URL http://www.sciencedirect.com/science/article/pii/0009250988850516

[23] A. Y. Tong, A numerical study on the hydrodynamics and heat transfer of a circular liquid jet impinging onto a substrate, Numerical Heat Transfer, Part A: Applications 44 (1) (2003) 1–19. arXiv:https://doi.org/10.1080/713838171, doi:10.1080/713838171.
URL https://doi.org/10.1080/713838171

[24] J. Stevens, B. W. Webb, Local Heat Transfer Coefficients Under an Axisymmetric, Single-Phase Liquid Jet, Journal of Heat Transfer 113 (1) (1991) 71–78. arXiv:https://asmedigitalcollection.asme.org/heattransfer/article-pdf/113/1/71/5910716/71_1.pdf, doi:10.1115/1.2910554.
URL https://doi.org/10.1115/1.2910554

[25] D. B. Coveney, Cutting ice with high pressure water jets (decoupage de la glace par de puissants jets d'eau)., Tech. Rep. ADA106985, NATIONAL

RESEARCH COUNCIL OF CANADA OTTAWA (ONTARIO) DIV OF MECHANICAL ENGINEERING, NATIONAL RESEARCH COUNCIL OF CANADA OTTAWA (ONTARIO) DIV OF MECHANICAL ENGINEERING, Ottawa (Jul. 1981).
URL http://www.dtic.mil/docs/citations/ADA106985

[26] R. J. Moffat, Describing the uncertainties in experimental results, Experimental Thermal and Fluid Science 1 (1) (1988) 3–17.

[27] S. van der Walt, J. L. Schönberger, J. Nunez-Iglesias, F. Boulogne, J. D. Warner, N. Yager, E. Gouillart, T. a. Yu, scikit-image: image processing in python, PeerJ 2 (2014) e453. doi:10.7717/peerj.453.
URL https://doi.org/10.7717/peerj.453

[28] N. Otsu, A threshold selection method from gray-level histograms, IEEE Transactions on Systems, Man, and Cybernetics 9 (1) (1979) 62–66. doi:10.1109/TSMC.1979.4310076.

[29] C. Li, C. Lee, Minimum cross entropy thresholding, Pattern recognition 26 (4) (1993) 617–625.

[30] Jui-Cheng Yen, Fu-Juay Chang, Shyang Chang, A new criterion for automatic multilevel thresholding, IEEE Transactions on Image Processing 4 (3) (1995) 370–378. doi:10.1109/83.366472.

[31] X. Liu, V. Lienhard, J. H., J. S. Lombara, Convective Heat Transfer by Impingement of Circular Liquid Jets, Journal of Heat Transfer 113 (3) (1991) 571–582. arXiv:https://asmedigitalcollection.asme.org/heattransfer/article-pdf/113/3/571/5553188/571_1.pdf, doi:10.1115/1.2910604.
URL https://doi.org/10.1115/1.2910604

[32] E. Guyon, J.-P. Hulin, P. L., Hydrodynamique physique, 3rd Edition, Savoirs Actuels. Physique, EDP Sciences, Ulis, France, 2012, Ch. Transports couplés. Couches limites laminaires, pp. 491 – 561.

[33] G. James, D. Witten, T. Hastie, R. Tibshirani, An Introduction to Statistical Learning: with Applications in R, Springer New York, New York, NY, 2013, Ch. Linear Regression, pp. 59–126. doi:10.1007/978-1-4614-7138-7_3.
URL https://doi.org/10.1007/978-1-4614-7138-7_3

[34] A. K. Biń, Gas entrainment by plunging liquid jets, Chemical Engineering Science 48 (21) (1993) 3585–3630.

8. Appendix: Absolute uncertainties on experimental variables

Exp. ref.	$\Delta V_{j,imp}$ $m.s^{-1}$	Δd_{imp} μm	Δt_{pe} s	ΔRe_{imp} $\times 10^3$	ΔPr	ΔB	ΔWe_{imp}
11	0.10	170	0.05	1.3	0.29	0.03	26
12	0.12	91	0.04	2.0	0.29	0.03	65
13	0.20	96	0.24	3.7	0.29	0.03	217
14	0.29	98	0.56	5.5	0.29	0.03	469
15	0.37	99	0.64	7.3	0.29	0.03	829
21	0.14	37	0.02	2.4	0.16	0.04	34
22	0.13	100	0.24	2.5	0.16	0.04	60
23	0.23	97	0.08	5.2	0.16	0.04	252
24	0.32	98	0.22	7.6	0.16	0.04	533
25	0.40	99	0.40	9.9	0.15	0.04	898
31	0.06	120	0.17	1.4	0.10	0.04	15
32	0.12	94	0.17	3.2	0.11	0.04	75
33	0.23	98	0.42	6.7	0.10	0.04	278
34	0.34	99	0.58	10	0.09	0.04	594
35	0.38	99	0.43	12	0.09	0.04	913

Table 4: Detailed summary of the absolute uncertainties linked to the important parameters reported in table 2. Exp. ref. is the experiment reference. $V_{j,imp}$, d_{imp}, Re_{imp}, Pr, B, We_{imp} are jet temperature, velocity, diameter, Reynolds number, Prandtl number, melting number B and Weber number at impact. H is jet drop height. t_{pe} is the time of transition to pool effect. The absolute uncertainty on H is arround 1 mm and the one on $T_{0,j}$ is of 2 ^oC.

9. Appendix: Complementary data used for regression

T_j °C	V_j $m.s^{-1}$	d m	V_f $m.s^{-1}$
70	4.77	1.0×10^{-3}	1.0×10^{-2}
50	4.77		7.0×10^{-3}
30	2.47		3.1×10^{-3}
	4.77		5.0×10^{-3}
	7.07		5.5×10^{-3}
	9.37		7.1×10^{-3}
50	2.49		4.6×10^{-3}
	4.72		6.93×10^{-3}
	7.02		9.12×10^{-3}
	9.34		1.07×10^{-2}
70	2.71		6.06×10^{-3}
	5.20		9.92×10^{-3}
	7.77		1.24×10^{-2}
	10.4		1.48×10^{-2}
30	2.48	1.2×10^{-3}	3.57×10^{-3}
	4.81		4.34×10^{-3}
	7.18		5.17×10^{-3}
	9.57		6.09×10^{-3}
50	2.66		4.67×10^{-3}
	5.15		6.62×10^{-3}
	7.70		8.53×10^{-3}
	10.3		1.00×10^{-2}
70	2.82		6.35×10^{-3}
	5.51		8.81×10^{-3}
	8.24		1.07×10^{-2}
	11.0		1.22×10^{-2}

Table 5: Complementary data obtained during preliminary tests.